

Investigating the Relationship Between In-Process Quality Metrics and Mechanical Response in the L-PBF Process

Bradley J. Sampson^{1,2}, Courtney Morgan-Barnes^{1,2}, Ryan Stokes^{1,2}, Haley Doude², and Matthew W. Priddy^{1,2}

¹Department of Mechanical Engineering, Mississippi State University, Mississippi State, MS 39762

²Center for Advanced Vehicular Systems, Mississippi State University, Starkville, MS 39759

Abstract

Laser powder bed fusion (L-PBF) additive manufacturing is a process that utilizes a high-powered laser to build near net-shaped parts in a layer-by-layer fashion using metal powder as the feedstock material. Traditionally, the analysis of L-PBF produced parts has relied solely on post-build characterization to understand the relationship between the printing process and the final mechanical properties. Recent developments of in-process quality assurance systems, such as Sigma Additive Solutions' PrintRite3D, can measure in-process thermal signatures and melt pool disturbances in real-time. This research aims to examine the relationship between process parameters (e.g., scan strategy, scanning speed, and layer thickness) and in-process quality metrics (IPQMs) captured by the PrintRite3D system on a Renishaw AM400. The mechanical response of multiple part geometries (NIST residual stress bridges, single-arched bridges) and build materials (Ti6Al4V) includes residual stress deflection and hardness; the results are compared with the IPQMs.

Keywords

Laser powder bed fusion, selective laser melting, in-situ process monitoring, Ti6Al4V, thermal monitoring, additive manufacturing

Introduction

Laser powder bed fusion (L-PBF) is a layered process that uses a high-powered laser to fuse metal powder into a desired geometry. To manufacture a part using L-PBF, a computer-aided design (CAD) model of the desired geometry must first be created. This geometry is then sliced into a layered format, and the toolpath of the laser is exported as g-code that can be read by the machine. To begin the manufacturing process, a substrate of the corresponding material to be printed is mounted to the build platform, the build chamber is inerted with argon, and the substrate is heated to 170°C. A thin layer of metal powder is then spread across the substrate surface, followed by melting of the powder with the laser based on the layer dimensions. When a layer of the part has finished being scanned with the laser, the elevator height decreases by the layer thickness, and a new layer of powder is spread with the recoater blade. The process is repeated until all layers of the sliced CAD geometry have been scanned with the laser, and the result is a physical metal part. The process is advantageous to various industries including automobile, aerospace, and biomedical industries because it can produce complex geometries that cannot be accomplished through traditional manufacturing techniques, reduce material waste, decrease production times, and build functionally graded materials [1]. Even though the L-PBF process is a repeated cycle, melt pool instability can play a major role in the quality and repeatability of the

part being manufactured [2]. The process can be modified by changing various process parameters including laser power, scanning speed, scan strategy, hatch spacing, layer thickness, etc., which will all result in changes to the microstructure and mechanical response; however, keeping these parameters constant can still result in microstructural changes due to melt pool instability. The physical nature of a traveling melt pool can result in part defects such as balling, lack of fusion, or keyholing, but these defects typically are not discovered until post-build characterization is performed, such as X-ray Computed Tomography (CT). Performing post-build characterization can be a time consuming and cost prohibitive task, impacting the acceptance of L-PBF as an industry standard for part production.

One way to characterize the physical aspects of a part before the quality inspection process is through in-situ process monitoring. Various optical hardware setups, such as an IR camera, have been used to monitor the melt pool and detect changes in the laser temperature and emissivity [4-6]. Sigma Additive Solutions has developed an in-situ thermal monitoring software named PrintRite 3D that uses coaxial emission spectroscopy to identify thermal signatures and melt pool disturbances [3]. The system consists of two on-axis single point photodetectors that are optically aligned with the laser. Both photodetectors are positioned behind a bandpass filter, where the thermal signatures are captured from two different wavelengths. The photodiode arrangement can be seen in Figure 1.

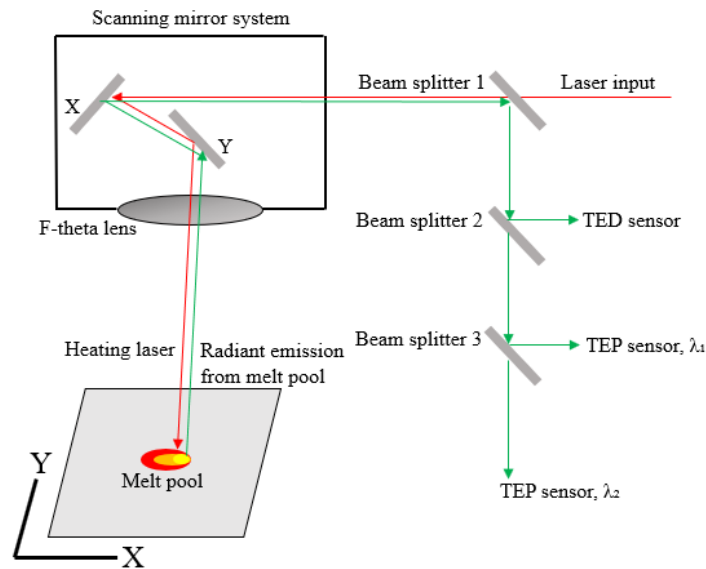


Figure 1: Dual photodiode system used by Sigma Additive Solutions’ PrintRite 3D (Adapted from [4])

The analog signals from these photodetectors are stored as floating-point values called in-process quality metrics (IPQMs) and can indicate inconsistencies and anomalies that arise during the printing process. Two IPQMs that can be recorded during the build process are Thermal Emission Density (TED) and Thermal Energy Planck (TEP) [7]. TED represents the process parameters that are input into the powder bed through the laser parameters, and how the material responds to those parameters. TEP represents the temperature of the region that the energy is being applied to [10]. While work has been completed to calibrate these thermal signatures into actual temperature values [4], [10], the mechanical response associated with changes in these signatures has not been analyzed.

This study aims to determine a relationship between the input process parameters and IPQMs captured by the PrintRite 3D system on a Renishaw AM400. Process parameters including scan strategy, scanning speed, and layer thickness are varied among three separate builds of Ti6Al4V specimens, and the specimens are analyzed through post-build characterization techniques including residual stress deflection and microhardness indentation. The average values of TED and TEP that are recorded for each part are compared with the post-build analysis results.

Methods

Build and process parameter selection

Three builds of varying process parameters were completed using Ti6Al4V powder in a Renishaw AM400. The process parameters used for each build are shown in Table 1. The process parameters used for build 2 are the nominal set for Ti6Al4V powder provided by the manufacturer. Build 1 differed from build 2 by reducing the layer thickness from 60 μm to 30 μm , and build 3 differed from build 2 by reducing the scan speed from 1333 mm/s to 857 mm/s. Each build contained nine NIST bridges, single-arched bridges, and 1" cubes, for a total of 27 parts on each substrate. An image of one of the substrates containing these geometries is shown in Figure 2. The geometries were printed with three iterations of each scan strategy (stripe, meander, and checkerboard). In this study, the NIST bridges were utilized for residual stress deflection, and the single-arched bridges were analyzed for hardness.

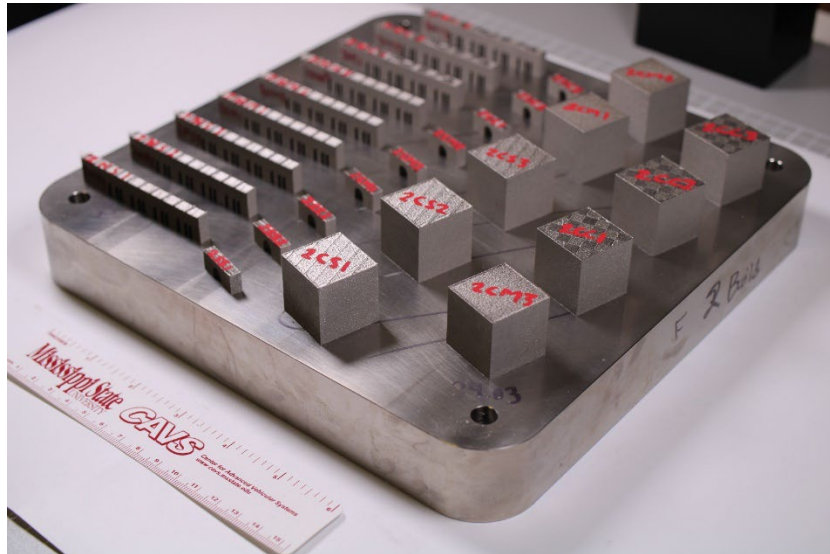


Figure 2: Substrate containing as built NIST bridges, single arched bridges, and contour cubes

Table 1: Process parameters used for each build

Build #	Scan Strategy	Layer Thickness (μm)	Power (W)	Point Distance (μm)	Exposure Time (μs)	Scan Speed (mm/s)	Spot Size (μm)	Hatch Spacing (μm)
1	Stripe	30	200	80	60	1333	65	70
	Meander	30	200	80	60	1333	65	70
	Checkerboard	30	200	80	60	1333	65	70
2	Stripe	60	200	80	60	1333	65	70
	Meander	60	200	80	60	1333	65	70
	Checkerboard	60	200	80	60	1333	65	70
3	Stripe	60	200	60	70	857	65	70
	Meander	60	200	60	70	857	65	70
	Checkerboard	60	200	60	70	857	65	70

Deflection Measurements

The residual stress distortion was measured using the deflection method for nine NIST bridges, including one of each scan strategy from each build. The bridges were sectioned away from the other specimens on the substrate using wire electrical discharge machining (WEDM). An initial contour scan of each bridge was taken using a Keyence VR-5000 optical profilometer, and the as-built height of each ridge at the top of the NIST bridge was measured by taking a surface area measurement of each ridge location with the substrate surface set as a reference plane, revealing the maximum height. After the initial measurements were taken, the bridges were sent off to have an additional cut made using WEDM to separate the legs of the bridge from the substrate, allowing the bridge to deflect upward due to residual stress relaxation. The measurement process was repeated for the deflected bridges, and the deflection for each bridge was calculated by subtracting the initial heights from the final heights. Figure 3 shows the measurement location of each ridge labeled 1-10.

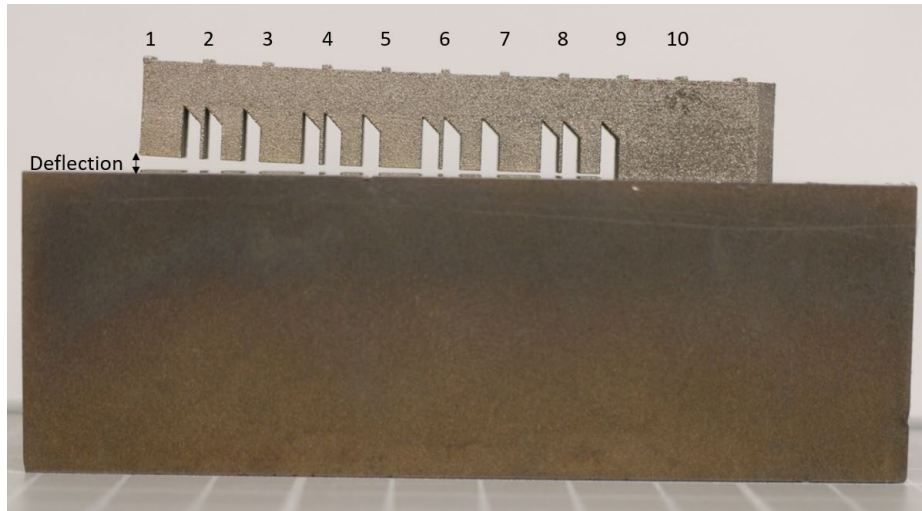


Figure 3: Ridge locations for each NIST bridge

Hardness Testing

The single-arched bridges were analyzed for Vickers hardness using a Wilson VH3100 microhardness indenter. Hardness measurements were taken of both the top (X-Y plane) and side (Y-Z) plane. The specimens were removed from the substrate using a diamond saw, followed by mounting and polishing to a 3 μ m surface roughness. Three specimens from each build (one of each scan strategy) were tested using the HV 0.5 scale. The indentations were created in a grid that spanned the surface with an indent spacing of 0.75 mm and a distance to the edge of 0.4 mm, resulting in approximately 115 indents for the top surface and 200 indents for the side surface. The indentations had a load of 500 gf and a dwell time of 10s.

Thermal Data Collection

The thermal history of each part was recorded during the build process using the PrintRite3D system. The thermal data is stored as images that display the spatially dependent IPQMs across a layer of each part where each pixel represents a single data point for that layer (Figure 4). The data can also be exported as comma separated value (.csv) files that contain the mean, maximum, and minimum of the IPQMs for each layer of each part. The average and standard deviation of the TED and TEP values were calculated and plotted in Figures 53 and 64.

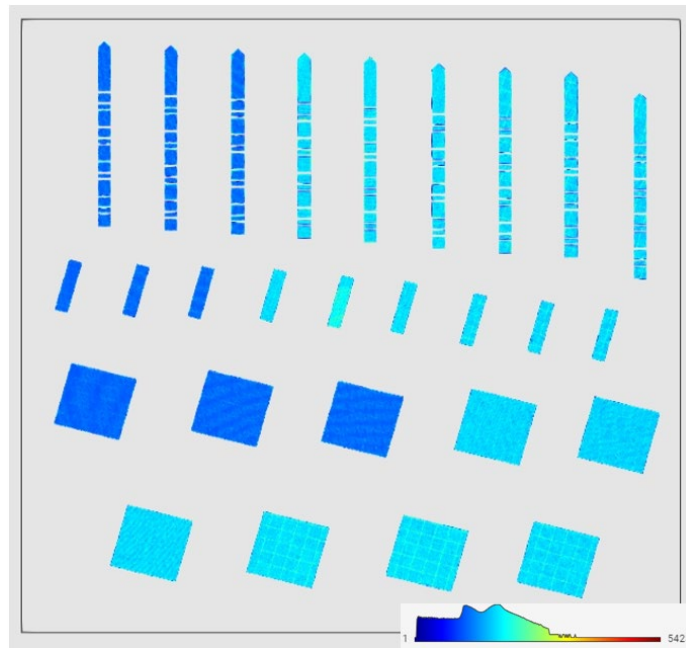


Figure 4: Layer image of TED values from build 2

Results and Discussion

The average TED values recorded for NIST bridges of each scan strategy are presented in Figure 53. There is a significant decrease in the TED values recorded for the stripe scan strategy in build 1 compared to the meander and checkerboard scan strategies. Also, the TED values recorded from each scan strategy in build 3 are significantly larger than those recorded from both builds 1 and 2.

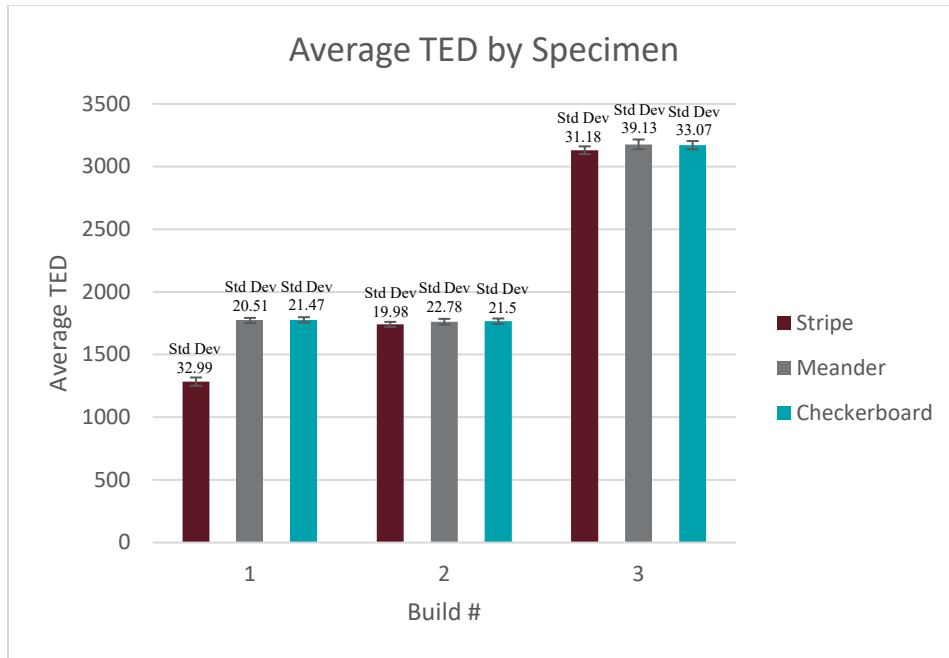


Figure 53: Average TED of NIST bridges for each process parameter variation

In Figure 64, the average TEP values recorded for NIST bridges of each scan strategy are presented. There is a significant increase in the average TEP recorded for the stripe scan strategy in build 1 compared to the average values recorded for the meander and checkerboard scan strategies. Also, the TEP values recorded for each scan strategy in build 3 are significantly lower than those presented for builds 1 and 2.

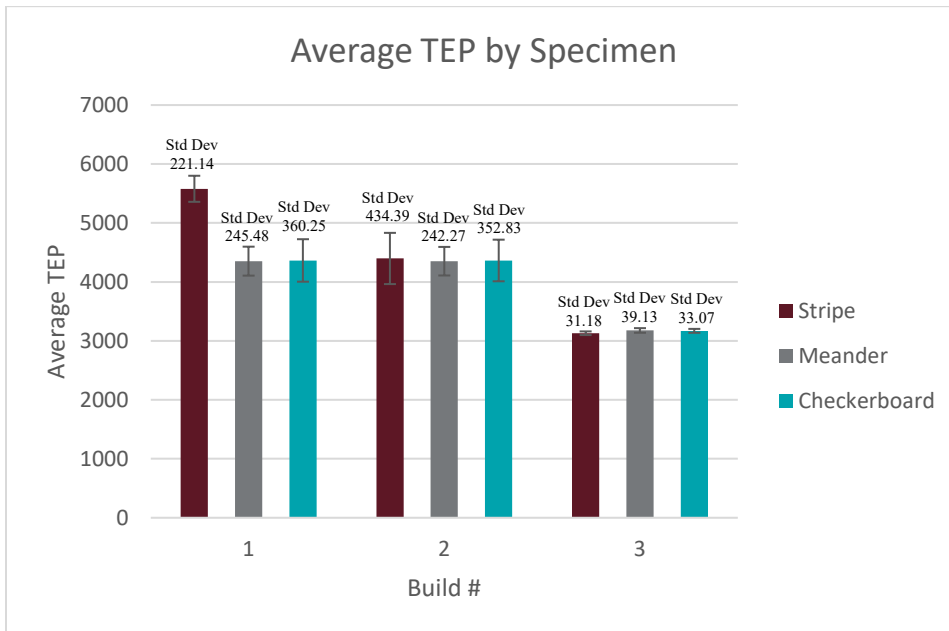


Figure 64: Average TEP of NIST bridges for each process parameter variation

Deflection Results

The resulting change in height (deflection) of each NIST bridge after being partially removed from the substrate is shown in Figure 73. The deflection presented for each specimen was taken from the end of the bridge corresponding to ridge #1 in Figure 32.

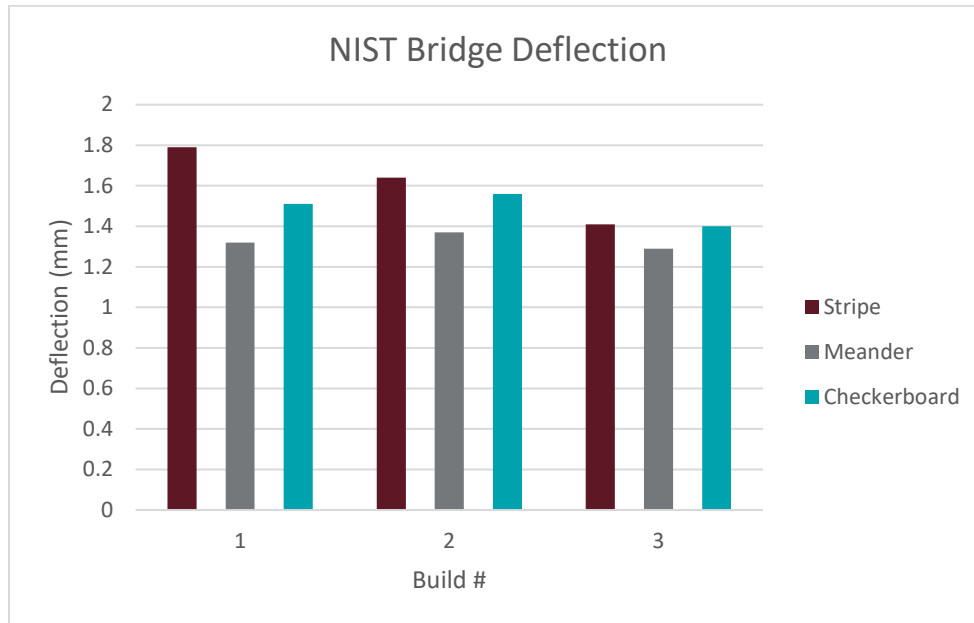


Figure 75: Deflection of NIST bridges by build number and scan strategy

Based on the results of Figure 75, the meander scan strategy (average deflection of 1.33 mm) consistently results in the greatest reduction of residual stresses, followed by checkerboard (average deflection of 1.49 mm) and stripe (average deflection of 1.61 mm). Also, build 3 (average deflection of 1.37 mm) resulted in an overall reduction in residual stress compared to build 1 (average of 1.54 mm) and build 2 (average deflection of 1.52 mm).

Hardness Results

In Figure 86, the Vickers hardness of the single-arched bridges built using process parameters from build 1 is shown as a contour plot for: (a) stripe scan strategy, (b) meander scan strategy, and (c) checkerboard scan strategy. The contour plot is presented for hardness measurements taken on the side (Y-Z plane) of each specimen. The average value for Vickers hardness and the standard deviation of each specimen is shown to the left, and the contour map legend is shown to the right.

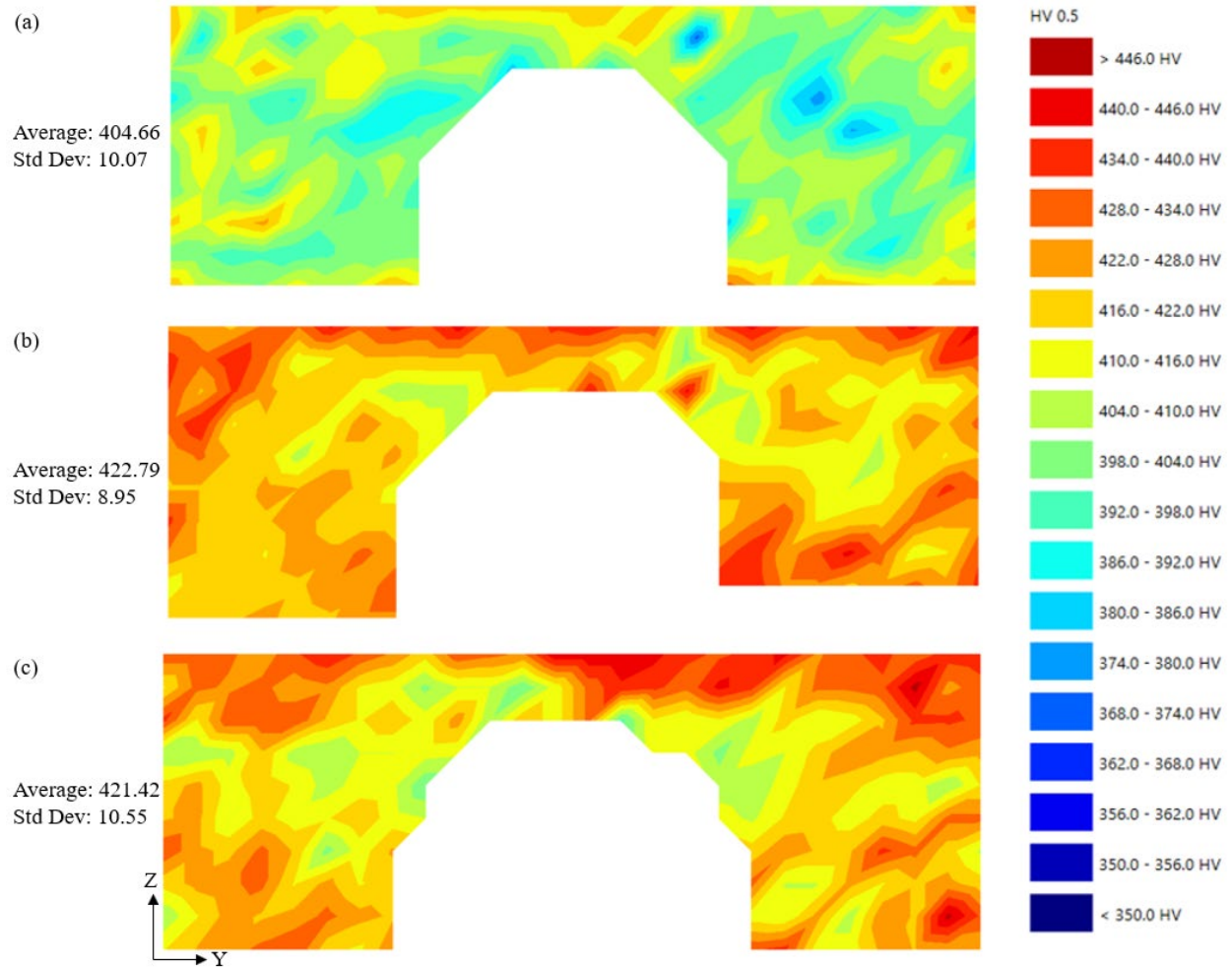


Figure 86: Vickers hardness results from build 1 by scan strategy: (a) Stripe, (b) Meander, and (c) Checkerboard

Each scan strategy results in a large variation of hardness across the surface (14.5 % for stripe, 9.7 % for meander, and 12.3 % for checkerboard). The meander scan strategy had the highest hardness value at 422.7 HV followed closely by checkerboard at 421.4 HV. The average hardness recorded for the stripe scan strategy was significantly lower at 404.7 HV. The hardness for all three specimens seems to be higher at the edges and lower in the middle. In Figures 97 and 108, the TED and TEP values recorded from each layer of the single-arched bridges produced in build 1 are shown. The lower TED values and higher TEP values are repeatedly seen for the stripe scan strategy throughout the building process.

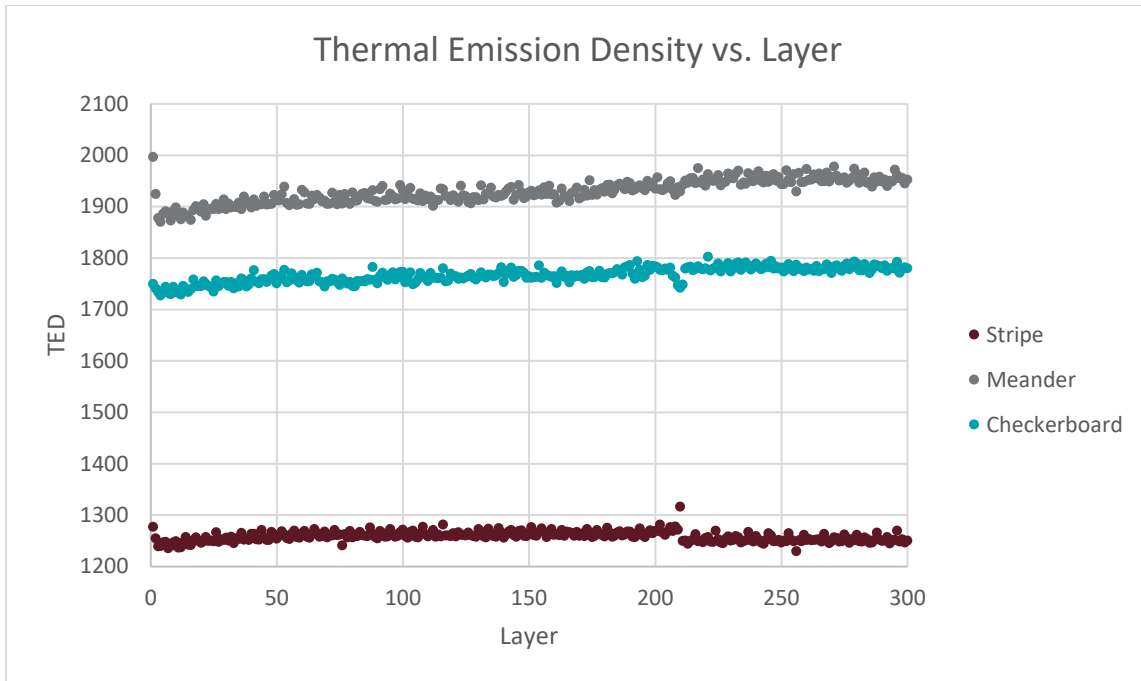


Figure 97: TED vs. layer for single arched bridges built using build 1 process parameters

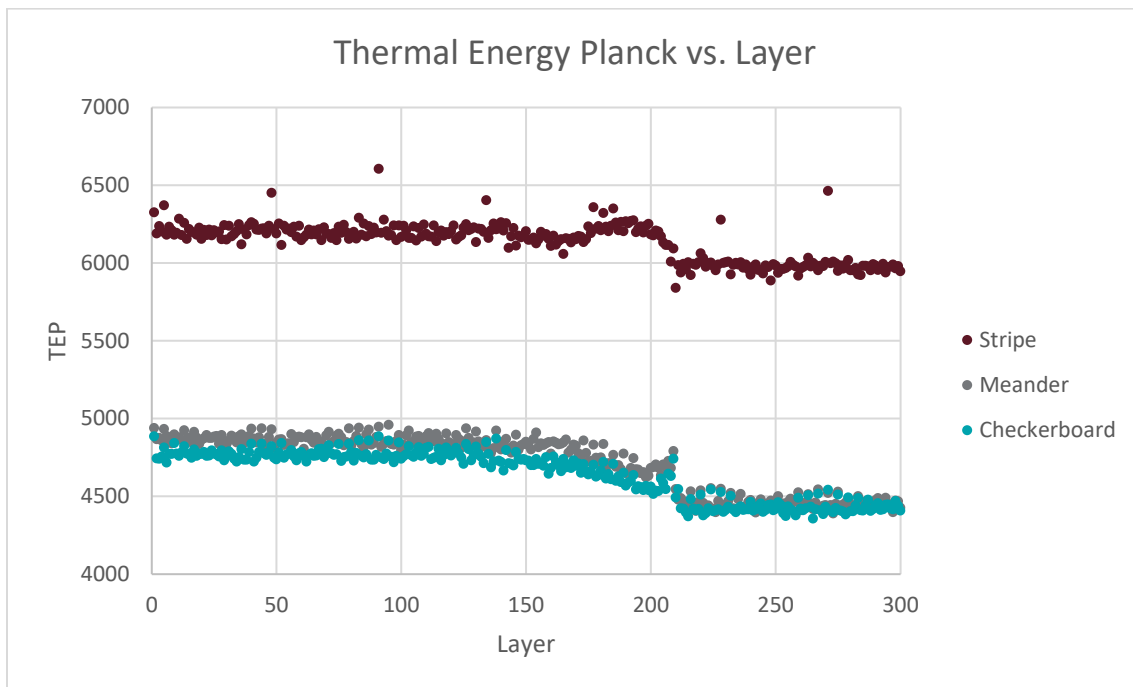


Figure 108: TEP vs. layer for single arched bridges built using build 1 process parameters

Based on the results presented, there is a correlation between IPQMs and mechanical response. The average TED and TEP values recorded for each part seem to be inversely proportional to each other (as shown in figures 53 and 64). The stripe specimen from build 1 had the largest deflection (Figure 75), and it also had the highest average TEP (Figure 64) and the

lowest average TED (Figure 53). This is also supported by the fact that build 3 had the lowest average deflection but the highest average TED and lowest average TEP across the specimens of each scan strategy. This can be attributed to the reduction in scanning speed in build 3 from 1333 mm/s to 857 mm/s. When comparing the hardness results to the IPQMs, we can see that an increase in TEP and a decrease in TED results in a lower hardness, which is the case for the stripe specimen in Figure 86a. Also, a sharp decrease in TEP values can be observed for each scan strategy at approximately layer 205 due to the increasing cross section of the layer being scanned as the bridge geometry merges from two rectangles into one (Figure 108). The correlations that have been observed between IPQMs and mechanical response can be helpful in establishing a process-property relationship for materials manufactured using L-PBF. Further work such as X-ray CT could be beneficial to this relationship if regions of porosity are compared to regions where there is a significant change in the IPQMs.

Conclusion

In this work, the thermal history in the form of layer dependent photodiode signals of Ti6Al4V parts built using L-PBF was compared based on variations in process parameters including scan strategy, scanning speed, and layer thickness. Also, the mechanical response of printed geometries including residual stress deflection and hardness were analyzed. It was found that higher TEP values and lower TED values can result in a larger residual stress deflection and a lower hardness. Further work is needed to provide a more detailed analysis of the thermal history of each part. Visualizing the spatial change in IPQMs across each layer of the entire build height would be beneficial, rather than relying on the average values for each layer.

Acknowledgements

This work is part of an ongoing Block-Gift program titled “Towards the Prediction and Reduction of Residual Stresses in Additively Manufactured Ti-6Al-4V” and awarded by the II-VI Foundation in support of Graduate and Undergraduate research on scientific topics of interest and importance.

References

- [1] “What is Powder Bed Fusion? Process Definition and Advantages - TWI.” <https://www.twi-global.com/technical-knowledge/faqs/what-is-powder-bed-fusion> (accessed Jun. 08, 2022).
- [2] B. Wu *et al.*, “In situ monitoring methods for selective laser melting additive manufacturing process based on images — A review,” *China Foundry*, vol. 18, no. 4, pp. 265–285, Jul. 2021, doi: 10.1007/s41230-021-1111-x.
- [3] S. Betts, L. Jacquemetton, and D. M. Piltch, “The relationship between In-Process Quality Metrics & Computational Tomography,” p. 11.
- [4] B. Diehl, A. Castro, L. Jacquemetton, and D. Beckett, “Thermal Calibration of Ratiometric, On-Axis Melt Pool Monitoring Photodetector System Using Tungsten Strip Lamp,” *Mater. Eval.*, vol. 80, no. 4, pp. 64–73, Apr. 2022, doi: 10.32548/2022.me-04271.
- [5] M. Strantza *et al.*, “Coupled experimental and computational study of residual stresses in additively manufactured Ti-6Al-4V components,” *Mater. Lett.*, vol. 231, pp. 221–224, Nov. 2018, doi: 10.1016/j.matlet.2018.07.141.

- [6] F. G. Fischer, N. Birk, L. Rooney, L. Jauer, and J. H. Schleifenbaum, "Optical process monitoring in Laser Powder Bed Fusion using a recoater-based line camera," *Addit. Manuf.*, vol. 47, p. 102218, Nov. 2021, doi: 10.1016/j.addma.2021.102218.
- [7] A. M. Öge, N. Durlu, H. Kizilok, H. Ö. Ünver, A. Kiliç, and O. Eroğul, "ADDITIVE MANUFACTURING OF TITANIUM ALLOYS," p. 20, 2016.
- [8] M. Aminzadeh and T. Kurfess, "In-Situ Quality Inspection of Laser Powder-Bed Fusion Using High-Resolution Visual Camera Images," p. 16.
- [9] R. J. Williams *et al.*, "In situ thermography for laser powder bed fusion: Effects of layer temperature on porosity, microstructure and mechanical properties," *Addit. Manuf.*, vol. 30, p. 100880, Dec. 2019, doi: 10.1016/j.addma.2019.100880.
- [10] R. Yavari *et al.*, "Digitally twinned additive manufacturing: Detecting flaws in laser powder bed fusion by combining thermal simulations with in-situ meltpool sensor data," *Mater. Des.*, vol. 211, p. 110167, Dec. 2021, doi: 10.1016/j.matdes.2021.110167.